

Imaging performance of telescope mirrors for far-ultraviolet astronomy

Raymond G. Ohl, Timo T. Saha, Scott D. Friedman, Robert H. Barkhouser, and H. Warren Moos

We describe image testing, surface metrology, and modeling of telescope mirrors (0.5 m in diameter, $f/4.3$) for the Far Ultraviolet Spectroscopic Explorer (FUSE) satellite. Laboratory image testing of wavelengths in the visible, vacuum, and midultraviolet validated a theoretical analysis by use of the Optical Surface Analysis Code (OSAC). Our modeling is based on surface metrology, including measurements of figure, midfrequency error, and microroughness. This combination of metrology, out-of-band performance testing, and modeling verified that the mirrors would meet mission requirements. We use OSAC to predict the FUSE telescope's far-ultraviolet (90–120-nm) point-spread function and assess its effect on instrument efficiency. The mirrors have a 90% encircled energy diameter of 1.5 arc sec at $\lambda = 100$ nm. Including the effects of spacecraft pointing error, the mirrors have a predicted average slit transmission at $\lambda = 100$ nm of approximately 87% and 96% for the 1.25- and 4-arc sec-wide spectrograph slits, respectively, where the required transmissions are 50% and 95%. © 2000 Optical Society of America
OCIS codes: 110.6770, 120.4800, 220.4840, 260.7210, 120.3940, 110.2960.

1. Introduction

The Far Ultraviolet Spectroscopic Explorer (FUSE) is a NASA observatory that produces high-resolution ($\lambda/\Delta\lambda = 20,000$ – $25,000$) spectra of astrophysical targets over a 90.5–118.7-nm bandpass, utilizing a high effective area and a detector with a low background.^{1–3} The satellite was launched from Cape Canaveral Air Station on 24 June 1999 aboard a Boeing Delta II 7320-10 rocket for a 3-year mission. The FUSE project is managed at the Center for Astrophysical Sciences of the Johns Hopkins University (JHU), and all science and mission operations are controlled from JHU.

The instrument consists of four independent Rowland circle spectrographs. Each spectrograph chan-

nel is illuminated by its own normal-incidence, off-axis parabolic mirror. The mirrors are rectangular, each with a 352 mm \times 387 mm clear aperture, 2245-mm focal length, and approximately 5.5° off-axis angle.⁴ The Zerodur blanks were lightweight open back prior to figuring—approximately 70% of the substrate material was removed, leaving a 7.5-mm-thick face sheet and a final mass of approximately 7.7 kg. Each mirror is semikinematically mounted to a set of three actuators that provide in-flight tip, tilt, and focus control. The optical coatings are tailored such that the instrument effective area is optimized across the bandpass in the combined spectrum. Two mirrors are coated with ion-beam-sputtered silicon carbide (SiC), and the remaining two are coated with lithium fluoride (LiF) over aluminum (Al; Al:LiF), for maximum reflectivity over 90.5–110.3 nm and 98.0–118.7 nm, respectively.^{5–7} Five mirrors were fabricated—four flight mirrors and one SiC-coated spare.

The mirror subsystem has the following imaging requirement: The mirrors must focus 90% of the total energy from a point source at $\lambda = 100$ nm within a 1.5-arc sec diameter, which corresponds to a diameter of 16 μ m in the focal plane. This criterion ensures adequate slit transmission and spectrograph resolution. Each spectrograph channel is equipped with a 1.25 arc sec \times 20 arc sec, high-resolution entrance slit (HIRS); a 4 arc sec \times 20 arc sec, medium-

When this research was performed, R. G. Ohl (Raymond.G.Ohl@gssc.nasa.gov), S. D. Friedman, R. H. Barkhouser, and W. H. Moos were with the Department of Physics and Astronomy, Center for Astrophysical Sciences, Johns Hopkins University, Baltimore, Maryland 21218. R. G. Ohl was also with the Department of Astronomy, University of Virginia, Charlottesville, Virginia 22903, but he is now with NASA Goddard Space Flight Center, Greenbelt, Maryland 20771. T. T. Saha is with NASA Goddard Space Flight Center, Greenbelt, Maryland 20771.

Received 14 December 1999; revised manuscript received 21 March 2000.

0003-6935/00/254513-11\$15.00/0

© 2000 Optical Society of America

resolution slit (MDRS); and a 30 arc sec \times 30 arc sec, high-throughput slit. Instrument-level imaging requirements [which include the effects of mirror point-spread function (PSF), mirror misalignment relative to the spectrograph, and spacecraft pointing error] call for 50% transmission through the HIRS and 95% transmission through the MDRS at all wavelengths in the FUSE bandpass.⁸ We define slit transmission as the relative enslitted energy between the high-throughput slit and the HIRS or MDRS, assuming a point source with a flat spectrum.

Silicon Valley Group, Inc., Tinsley Laboratories⁹ (Tinsley) weight-relieved the blanks, figured the mirrors into parabolas, bonded the mirror mounting flexures, and performed most of the predelivery surface metrology (Section 2). After delivery of the substrates to JHU, the Optical Thin Film Laboratory at NASA Goddard Space Flight Center (GSFC) applied the optical coatings. The mirrors were then attached to mounting hardware and actuators at JHU and figure tested at each stage of assembly to monitor distortions from assembly-induced stress. A sixth qualification mirror with a spherical figure was fabricated first and preceded the five off-axis parabolas through assembly and environmental and optical testing. All mirrors experienced a peculiar assembly-induced distortion, which was the result of the epoxy that was used to bond the mounting flexures to the back of each mirror and the attachment of mounting hardware to these flexures.¹⁰ The assembly-induced distortion is nearly identical in amplitude and character for all the mirrors, producing a similar optical figure error.

Schedule constraints prevented a laboratory test of the imaging performance of the flight mirrors. However, the flight spare mirror, which has similar surface error, was fully characterized at several wavelengths longward of the FUSE bandpass: 435.8, 253.7, and 184.9 nm. We used the Optical Surface Analysis Code (OSAC)^{11,12} at GSFC to model the imaging performance of the spare mirror in the laboratory double-pass test setup. After validation of the OSAC model with the laboratory data, the modeling was extended with confidence to the flight mirrors and into the FUSE bandpass. Preliminary image testing and modeling of the spare mirror at $\lambda = 184.9$ nm were presented in a conference paper.¹³

We describe the OSAC modeling of one flight mirror (LiF2) and the spare mirror based on surface error characteristics and multiwavelength image testing of the spare. Although the FUSE mirrors have nearly identical figure error, they have different small-scale surface error. The small-scale surface error characteristics of the spare and the LiF2 are representative of the SiC- and Al:LiF-coated flight mirrors, respectively. Although executed on a tight budget and aggressive schedule, this program of testing and modeling provided a prediction of the on-orbit, far-ultraviolet (FUV; 90–120-nm) PSF for each mirror and verified that each unit met imaging requirements. Within errors set by systematic effects that limit the accuracy of our model, the mirrors meet the

subsystem encircled energy (EE) and instrument-level enslitted energy requirements (Subsection 4.D; Table 5).

Section 2 covers the surface error measurements performed after fabrication and at each stage of assembly and qualification. Section 3 details the laboratory image testing of the spare in a double-pass configuration. The OSAC modeling and its validation and the implications of the single-pass prediction for on-orbit performance are discussed in Section 4. A subsequent paper will compare in-flight telescope performance, including wide-angle scatter, with the results of this program.

2. Surface Metrology

A. Development of Fabrication Specifications

From the perspective of the modeling approach taken here, the FUV imaging performance of an optical surface can be considered in terms of two components to the PSF, combined in convolution at the image plane¹⁴: geometric broadening from light misdirected by large-scale departures from an ideal conic section and diffraction off topographic features with a spatial period ranging from as large as the system entrance pupil (aperture diffraction) to the smallest residual fabrication error (diffraction off surface irregularities; scatter).

The amplitude of the scatter component associated with small-scale surface error is a strong inverse function of wavelength in the UV, and the relative distribution of FUV scattered light in the focal plane is approximately proportional to the power spectral density (PSD) of mirror surface errors.^{15,16} The PSD is proportional to the square of the spatial frequency content of surface error by

$$\text{PSD}(f) \propto |F[s(q, p)]|^2, \quad (1)$$

where $s(q, p)$ is the surface height as a function of position (q, p) on the mirror and F is the Fourier-transform operator. We used the METDAT code¹⁷ to calculate the two-dimensional PSD. The program uses standard Fourier-transform techniques to calculate an azimuthally averaged PSD that can be fitted to a modified Lorentzian PSD model used in the OSAC scatter calculation (Section 4). This model is expressed as

$$\text{PSD}(f) = \sigma^2[(b - 2)f_0^{b-2}]/[2\pi(f_0^2 + f^2)^{b/2}], \quad (2)$$

where σ is the total rms surface error, b is the power-law falloff, and f_0 is a breakpoint in the spatial frequency f at which the PSD tends to change from a constant at low frequencies to a power-law falloff at higher frequencies.

Surface errors with spatial frequency f diffract energy to radii r in the focal plane as given by the following approximation to the grating equation:

$$r \approx \lambda f, \quad (3)$$

where λ is the wavelength of interest and r has units of radians. Normal incidence, first-order diffraction,

Table 1. Flight Mirror rms Surface Error

Spatial Period	Specification	FUSE Mirror				
		Spare	SiC1	SiC2	LiF1	LiF2
Figure (delivery) ^a	0.025	0.018 ± 0.001	0.026 ± 0.001	0.024 ± 0.001	0.027 ± 0.001	0.019 ± 0.001
Figure (postassembly) ^a	0.050	0.047 ± 0.002	0.047 ± 0.002	0.045 ± 0.002	0.051 ± 0.002	0.048 ± 0.002
Midfrequency ^b	20.0	11.8 ± 1.2	12.5 ± 1.6	11.6 ± 1.9	14.1 ± 1.8	18.5 ± 4.4
Microroughness ^b	10.0	3.7 ± 1.4	3.7 ± 1.1	4.8 ± 0.6	6.4 ± 1.4	9.8 ± 2.3

^aUnits are waves at λ = 632.8 nm.

^bUnits are in angstroms. The quoted errors reflect the 1σ spread in measurements for each mirror.

and small values of *r* have been assumed. Approximation (3) indicates that surface features with spatial frequency $\log f > -1.44$ (*f* is in units of inverse millimeters), or spatial period $1/f = \lambda_D < 27.5$ mm, would scatter light at λ = 100 nm outside of a circle 1.5 arc sec in diameter (see Section 1). Scatter is therefore important to the performance of the FUSE mirrors, and the specification of surface error over all relevant spatial frequencies is required. Fabrication specifications for the FUSE mirrors consisted of tolerances in rms surface error over three regimes of spatial period (Table 1): figure error, midfrequency error ($0.1 < \lambda_D < 10$ mm), and microroughness ($1 < \lambda_D < 100$ μm). The rms surface roughness over a given range in spatial frequency, *a*–*b*, is the square root of the 0th moment of the azimuthally averaged PSD:

$$\text{rms} = \left[2\pi \int_a^b f \text{PSD}(f) df \right]^{1/2}. \quad (4)$$

The total amplitude of surface errors on the FUSE mirrors was thus specified over nearly all spatial frequencies relevant to UV imaging, with midfrequency errors being the most critical for scatter in the vicinity of the imaging requirement. The PSD was not specified in detail, but limits were set on the total power between boundaries in the spatial period [Eq. (4)]. These tolerances were designed to produce mirrors that met the imaging requirement and were based on a modulation transfer function analysis and experience with mirror performance on the Solar Ultraviolet Measurements of Emitted Radiation experiment on the Solar Heliospheric Observatory.¹² We also confirmed the fabrication specifications using an OSAC scatter analysis (Subsection 4.A).¹⁸

B. Figure Error

Figure error was measured at Tinsley during fabrication and prior to delivery with a phase-shifting interferometer and at JHU before and after each stage of mirror assembly and qualification with a laser unequal-path interferometer in an autocollimation setup.¹⁹ The fabrication specification for figure error was $\text{rms} \leq 0.025\lambda$ at λ = 632.8 nm. All five mirrors essentially met specification on delivery (Table 1). After assembly and environmental testing, the mirrors all had approximately the same figure error, $\text{rms} \approx 0.050\lambda$ (Table 1; Section 1). This dis-

tortion is predominantly assembly-induced strain in the form of a large, Y-shaped ridge approximately 0.08λ high, with the shank of the Y oriented toward the mirror vertex and a depression approximately 3 cm wide and 0.04λ deep superimposed on each branch of the ridge (Figure 1).¹⁰ This degraded figure error was accepted in light of the cost and schedule implications associated with improving the figure by additional surface polishing or redesigning the mount. The larger geometric broadening does not have a drastic effect on the EE requirement (Subsection 4.D), especially for the SiC-coated mirrors, which have better small-scale surface error than the specification (Subsection 2.C).

The figures of the mirrors were observed to change over time during storage.¹⁰ The additional distortions were as large as $\pm 0.02\lambda$ in the rms figure error and took the form of changes in the amplitude of the overall Y-shaped distortion. These observations were confirmed by independent measurements on the spare mirror at Tinsely. The instability was roughly correlated with the moisture content or temperature of the air in the storage environment and implies a change in the stress in the mirror substrate caused by the epoxy that was used on the mirror flexure bond line (Section 1). No flight mirror distorted to better than approximately 0.025λ rms or worse than approximately 0.050λ rms. Shortly before integration with the rest of the FUSE instrument, all four flight

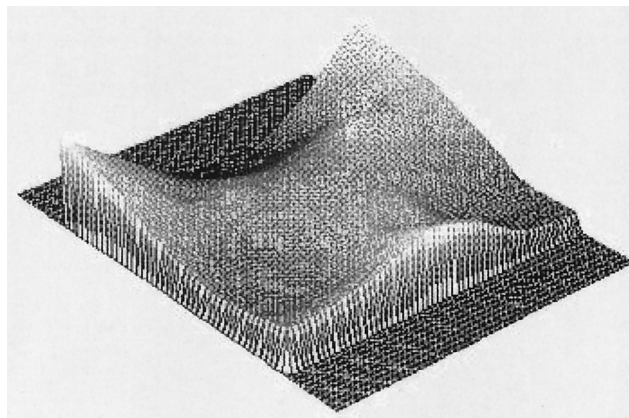


Fig. 1. Figure error common to the five FUSE mirrors. The height of the dominant Y-shaped distortion is approximately 0.08λ (λ = 632.8 nm). The mirror vertex is near the lower right edge of the aperture shown.

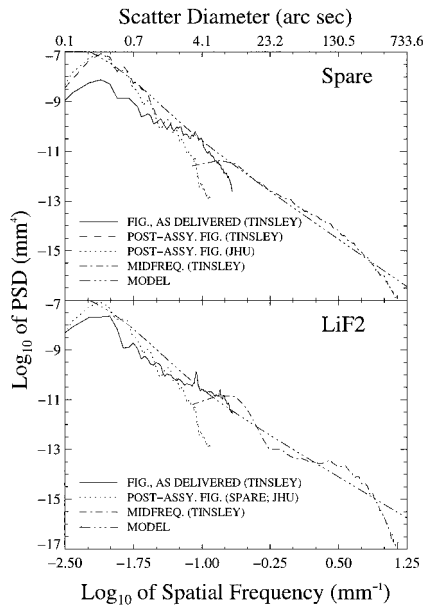


Fig. 2. Azimuthally averaged PSD of the mirror surface error for the spare and LiF2 flight mirrors (excluding microroughness error). Figure error PSD's are shown for the spare before delivery and after assembly. Because the mirrors have a similar figure error, the postassembly figure error PSD for the spare is also shown on the LiF2 plot. The two-component fit for the scattering calculation for each mirror is displayed as well. The model PSD for the spare is a good fit for the two SiC-coated flight mirrors, and the fit for the LiF2 is representative of both LiF-coated flight mirrors. Note the peak at $\log f \approx -1.05$ for LiF2. For the spare, the figure measurement that was made postassembly at Tinsley suffered from a high spatial frequency artifact, and the associated PSD (long dashed curves) is unreliable for $\log f > -1.5$. The upper horizontal axis is labeled for the diameter to which light at $\lambda = 100$ nm is scattered in first order by surface errors with a given spatial frequency, according to approximation (3).

mirrors had approximately 0.050λ rms figure error. The modeling presented here assumes that this is the on-orbit condition (Section 4). Although it is possible that the drying of the epoxy in the flight environment will alter the mirror figure, the laboratory data are not sufficient to predict with confidence the magnitude and sign of this change.

The azimuthally averaged PSD's of figure error prior to mirror delivery from Tinsley and postassembly are shown in Fig. 2 for the spare and the LiF2. These PSD's were generated from figure error data after the subtraction of a 37 Zernike polynomial fit for purposes of the modeling discussed in Section 4. The Zernike polynomial fit, $S(r)$, to the surface error data is an expansion of the form

$$S(r) = \sum_{l=0}^{\infty} d_l (l+1)^{1/2} R_l^0(r) + \sum_{l=0, m=1}^{\infty} [2(l+1)]^{1/2} R_l^m(r) \times [e_{lm} \cos(m\theta) + f_{lm} \sin(m\theta)], \quad (5)$$

where r and θ are polar coordinates in the mirror pupil; $R_l^m(r)$ are the Zernike polynomials; and d_l , e_{lm} , and f_{lm} are coefficients determined by the fit.¹² After subtraction of this model surface [i.e., $s(r, \theta) -$

$S(r)$], the PSD curves turn down at low spatial frequencies. The difference in slope between the pre-assembly and postassembly curves is a result of the distortion incurred during assembly. The Tinsley interferometer was much more sensitive to small-scale figure errors, so the figure PSD's from Tinsley connect smoothly with the midfrequency curves (Subsection 2.C). The JHU interferometer detected large-scale errors associated with assembly-induced distortions but did not have the sensitivity to confirm the Tinsley data for $\log f > -1.25$ (f is in units of inverse millimeters). However, where both instruments have good sensitivity, the measurements agree.

C. Midfrequency Error and Microroughness

Tinsley made interferometric measurements of mid-frequency error by sampling 10-mm-diameter patches on the surface of each mirror (Table 1). The midfrequency PSD's shown in Fig. 2 are averages of data from many sample locations on each mirror. These results were confirmed by use of a Bauer Model 100 profiler at GSFC.²⁰ The fabrication specification for midfrequency error was rms < 20 Å.

Tinsley also measured surface microroughness at several locations on each mirror (Table 1). The values are consistent with a linear extrapolation of the midfrequency PSD as shown in Fig. 2 to higher spatial frequencies. The fabrication specification for microroughness was rms < 10 Å. The average rms surface errors derived from the Tinsley midfrequency and microroughness data are listed for each mirror in Table 1, and the quoted error is the 1σ spread in values for each mirror. All five mirrors met their fabrication specifications for small-scale surface error (Table 1).

Note the peak at $\log f \approx -1.05$ (f is in units of inverse millimeters), or $\lambda_D \approx 11$ mm, in Fig. 2 for the flight mirror LiF2. This feature is the result of highly periodic residual fabrication errors. This gridlike pattern is distinct on the LiF-coated flight mirrors (with an amplitude of approximately 0.0025λ at $\lambda = 632.8$ nm), weaker in amplitude for the SiC-coated mirrors, and absent for the spare.

No surface roughness measurements were performed after the mirrors were coated. Studies of mirror samples before and after coating with SiC have found no change in roughness,²¹ and no change is observed with exposure to laboratory and space environments.²² Although the roughness of the Al:LiF-coated substrate is also unchanged after coating, the roughness increases with exposure to moisture, and there is a concurrent decrease in FUV reflectivity.²³ Prior to launch, the Al:LiF-coated surfaces were never exposed to a relative humidity greater than 50% at room temperature: We limited the total exposure to a nonpurged environment with a relative humidity $< 50\%$ to approximately 100 h. In addition, the mirrors were exposed to an environment of approximately 10% relative humidity for approximately 10 days. Mirror reflectivity was monitored during satellite integration and tested with a system

of witness coupons. Al:LiF mirror reflectivity at $\lambda = 106.7$ nm was approximately $70\% \pm 3\%$ after coating and decreased to approximately $67\% \pm 3\%$ shortly before launch.²⁴ This corresponds to a slight increase in surface roughness.²³ Our modeling assumes that mirror surface roughness did not change from values measured prior to coating.

3. Image Testing

Laboratory image testing of the spare served three purposes. First, it ensured that there were no gross problems with the mirror and confirmed expectations from figure testing. Second, it provided an empirical, but qualitative, picture of the PSF—e.g., image testing revealed that the geometric spot had primarily two components near focus, a tight core and a broad shoulder. The core is from light that is focused by regions with low surface errors (i.e., the three flat areas in the optical path difference map shown in Fig. 1), and the shoulder comes from rays that encounter the Y-shaped distortion.

Third and most important to the performance characterization, the image test validated the OSAC model of the mirror surface, which is based on fitting analytic functions to the metrology data (Sections 2 and 4). Agreement between the imaging data from the spare in the laboratory and the OSAC model of the experimental setup supports the validity of the model for single-pass performance predictions.

We performed image tests at three wavelengths ($\lambda = 435.8, 253.7, 184.9$ nm), which reveal surface errors with different spatial frequencies on the mirror. However, the signal-to-noise ratio obtained was not sufficient to place tight limits on scatter. The image test sampled only the brightest part of the intensity distribution, which is dominated by the effects of figure error and aperture diffraction, and thus primarily checked our treatment of figure error.

A. Optical Setup

Image testing of the spare was performed at JHU in a double-pass configuration similar to the setup for figure testing (Fig. 3).¹⁹ The source and pinhole aperture were slightly offset from the mirror's nominal focus in (folded) $-z$ and $+x$ (see Fig. 3 for coordinate definitions), incurring a negligible aberrated spot size²⁵ but sending the return beam into a detector. A mercury discharge pencil lamp permitted testing at $\lambda = 435.8, 253.7, 184.9$ nm. The optical path was purged with N_2 for testing at $\lambda = 184.9$ nm. The pinhole aperture was rotated about the y axis and mounted at a 45° angle with respect to the optical axis (Fig. 3), presenting in projection an $\sim 1 \mu\text{m} \times 6 \mu\text{m}$ object in x and y .

The surface error on the three flat mirrors used in this setup was potentially important to the system imaging performance (Table 2). The first fold mirror to encounter the source-pinhole output beam (Fold 1) was tested for figure and midfrequency error and microroughness at GSFC with a WYKO Model 400 interferometer,²⁶ the Bauer profiler, and a WYKO Model TOPO 3-D interferometer²⁷ with a $10\times$ mag-

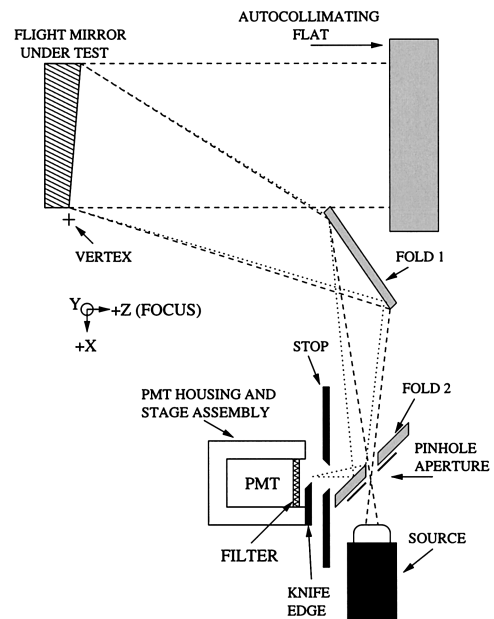


Fig. 3. Schematic of the image test setup for the spare in the clean-room facility at JHU (not to scale).

nification head, respectively. The large, autocollimating flat was tested for figure error and microroughness by the vendor.²⁸ The second fold mirror, which sends the return beam into the detector (Fold 2), was measured for figure error by the vendor²⁸ and measured for microroughness at GSFC with the WYKO Model TOPO 3-D interferometer. The EE curve for diameters sampled by the image test is dominated by the effect of figure error. Because these flats have much better figure than the spare and the test was not sensitive to scatter from small-scale, low-magnitude surface errors, we assumed that the flat mirrors have negligible surface error, and they are not considered in the modeling. Had the image test sampled scatter reliably beyond a few seconds of arc from the peak (Subsection 3.B), we would have had to consider the contribution from the flat mirrors in our modeling because the magnitudes of the small-scale errors on the flats and the spare are comparable.

B. Tomographic Imaging

The last flat mirror in the optical train (Fold 2) directs the return beam into a tomographic imaging detector (Fig. 3). The detector consists of a photomultiplier tube (PMT) and an interference filter for wavelength selection. The stopped-down entrance aperture of the PMT is partially covered by an opaque knife-edge (KE). The PMT and KE are mounted on a stage assembly that permits translation in x , y , and z and rotation about the optical axis (z).

After interferometric alignment,¹⁹ the source and pinhole are installed in place of the laser unequal-path interferometer. The detector assembly is then translated in the plane perpendicular to the optical axis, and the KE attenuates the spot. The PMT sig-

Table 2. Image Test Flat Mirror Surface Error (Figure 3)

Spatial Period	Flat Mirror		
	Fold 1 ^a (50 μm × 50 mm square)	Autocollimating Flat ^b (533.4-mm diameter)	Fold 2 ^c (25.4-mm diameter)
Figure (λ = 632.8 nm)	P-V ^d < 0.050λ	0.007λ rms, 0.049λ P-V	0.013λ rms, 0.056λ P-V
Midfrequency (Å)	~8	Not measured	Not measured
Microroughness (Å)	~7.5	2.34	~9

^aThe first fold flat to encounter the beam from the source pinhole.

^bThe large autocollimating flat.

^cThe second fold flat to encounter the beam (close to the return beam focus).

^dPeak-to-valley (P-V) figure error.

nal, recorded as a function of KE position, is the knife-edge distribution (KED), or the edge response. If $\rho(x, y, z)$ is the image as a function of x, y , and z (focus), then

$$\text{KED}(x', z_0) = \int_0^{x'} \int_{-\infty}^{+\infty} \rho(x, y, z_0) dy dx, \quad (6)$$

where x' indicates distance in the direction normal to the KE, z_0 is the position of the KE in focus, and it was assumed that the size of the detector entrance aperture is much greater (and the KE step size is much less) than the size of the spot. The negative derivative of the KED is the line-spread function (LSF; line response, or projection) associated with the return spot in the direction perpendicular to the KE:

$$\text{LSF}(x', z_0) = -\frac{d\text{KED}(x', z_0)}{dx'} = \int_{-\infty}^{+\infty} \rho(x', y, z_0) dy. \quad (7)$$

The detector focus is chosen by a comparison of successive LSF's generated in x for different z . The KED and LSF generated in the laboratory are discrete approximations to Eqs. (6) and (7).

After focusing, the KE is rotated in the focal plane about the optical axis (z), and we generated a new LSF by occulting the spot from a different azimuthal angle ϕ . ϕ is the angle between the normal to the KE and the $-x$ axis in the plane perpendicular to the optical axis (z). This is repeated for n angles ($n = 8-12$), evenly spaced in azimuth, generating a set of LSF's, $[\text{LSF}(x_i', z_0), i = 1, 2, 3, \dots, n]$. Sample LSF's in x and y ($\phi = 0^\circ$ and $\phi = 90^\circ$, respectively) are shown in Fig. 4 for tests at $\lambda = 253.7, 184.9$ nm.

The set $[\text{LSF}(x_i', z_0), i = 1, 2, 3, \dots, n]$ is processed with a filtered backprojection algorithm, which produces an image of the two-dimensional brightness distribution in the focal plane. This algorithm is a discrete approximation to the inverse Radon operator,²⁹⁻³¹

$$\rho'(x, y, z_0) = \sum_{i=1}^n B_i(F^{-1}\{wF[\text{LSF}(x_i', z_0)]\}), \quad (8)$$

where w is the ramp filter ($w = v$, where v is the spatial frequency associated with x'), B_i is the back-projection operator for the i th LSF, and ρ' is the

reconstructed image. [See, e.g., Rowland³⁰ and Bracewell³¹ for a complete discussion of the computer implementation of Eq. (8)]. This process amounts to a filtering of each one-dimensional LSF(x_i', z_0) with the ramp function w , then backprojecting, or smearing, the resulting one-dimensional function $F^{-1}\{wF[\text{LSF}(x_i', z_0)]\}$ across the image plane, creating an elongated ridge. These n , two-dimensional arrays, each with a ridge oriented at a different angle ϕ_i in the image plane, are summed entrywise. The resultant image, $\rho'(x, y, z_0)$, is a good approximation to the energy distribution in the focal plane (Fig. 5). The broadening associated with the PSF intrinsic to this tomography algorithm is negligible compared with the size of our expected return spot.³⁰

Artifacts appear in the reconstructed image from finite angular sampling. They are predominantly spokelike, azimuthal oscillations associated with the pileup of filtered LSF's.³⁰ The reconstructed images shown in Fig. 5 were scaled to emphasize these fea-

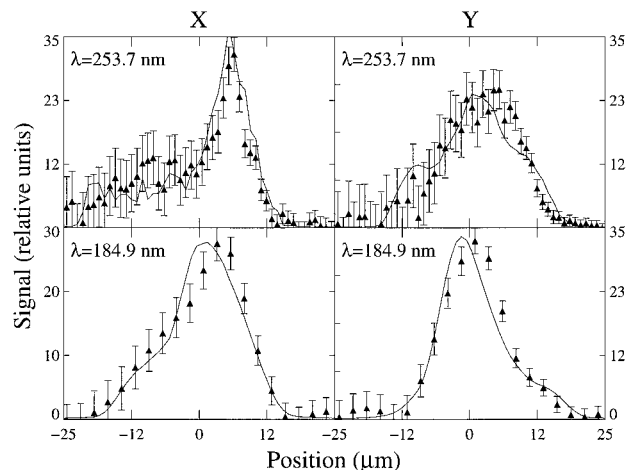


Fig. 4. LSF in x and y for two double-pass image tests (triangles). Note the concentrated core and broader shoulder, which is more evident in x . Synthetic LSF's generated from the corresponding OSAC output are also shown (solid curves). The error bars represent the 1σ deviation expected from Poisson statistics. The detector focus position and system alignment were different for each test (Table 4), so the shoulder appears more prominent at $\lambda = 253.7$ nm than at $\lambda = 184.9$ nm. The KE step size for the $\lambda = 184.9$ -nm test was larger than that for the $\lambda = 253.7$ -nm test, smoothing the derived LSF.

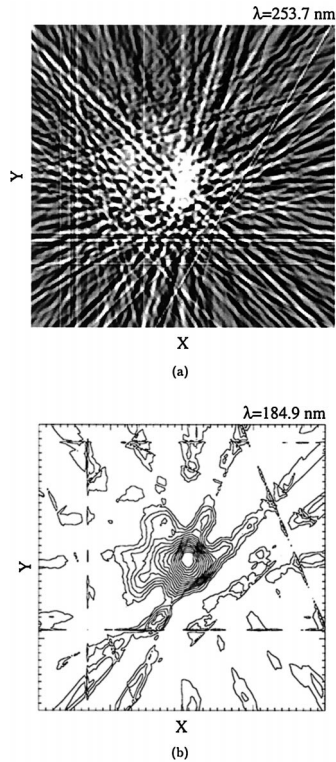


Fig. 5. (a) Linear gray-scale image of the reconstructed return spot for the $\lambda = 253.7$ -nm image test ($86 \mu\text{m} \times 86 \mu\text{m}$ field; $n = 12$). (b) Contour plot of the reconstructed return spot for the $\lambda = 184.9$ -nm image test ($91 \mu\text{m} \times 91 \mu\text{m}$ field; $n = 8$). The difference between adjacent surface brightness contours is constant.

tures, as well as to show the shoulder to the left ($-x$) of the more concentrated image core. The artifacts are less numerous but greater in amplitude for tests in which fewer angles ϕ are sampled (e.g., the $\lambda = 184.9$ -nm test had $n = 8$, whereas the $\lambda = 253.7$ -nm test had $n = 12$).

The goal of the tomographic reconstruction is to produce an image, $\rho'(x, y, z_0)$, on which synthetic, circular aperture photometry is performed and compared with corresponding OSAC EE calculations to validate the modeling (Section 4). These measurements are a discrete approximation to

$$EE(d = 2r', z_0) = \int_0^{r'} \int_0^{2\pi} \rho'(r, \phi, z_0) r \, d\phi dr, \quad (9)$$

where r and ϕ are polar coordinates in the image plane and r' represents radial distance from the center of the nested, circular apertures. The radial artifacts average out for the background subtraction associated with the application of Eq. (9), which azimuthally sums the reconstructed image. Differences between EE measurements performed on a synthetic test image and the corresponding processed image with reconstruction artifacts are negligible. EE curves are displayed in Fig. 6 for each test wavelength.

The EE data were of high quality for diameters less

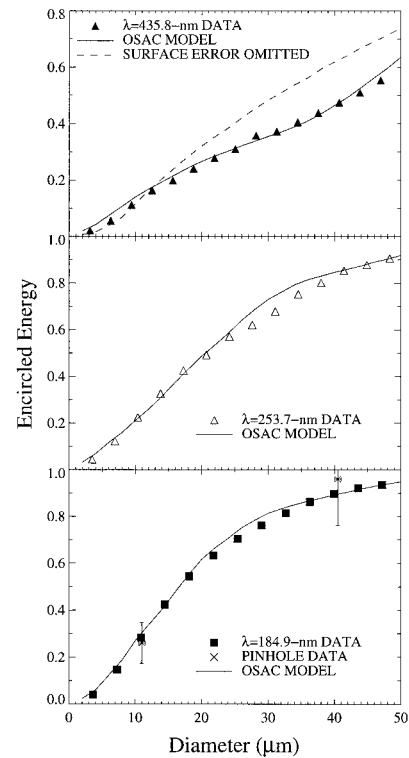


Fig. 6. EE curves for each laboratory image test. Statistical errors are smaller than the plotting symbols. The data are of poor quality beyond $50 \mu\text{m}$. For the $\lambda = 435.8$ -nm test, the most misaligned case—an OSAC prediction including the misalignment but assuming a perfect mirror surface—is also shown (dotted curve). The effect of figure error is well detected behind the given amount of misalignment (Table 4). Independently normalized pinhole EE measurements for $\lambda = 184.9$ nm are also shown.

than 4.6 arc sec ($<50 \mu\text{m}$). No measurements of near-angle scatter were made (e.g., at 5 – 100 -arc sec diameters). With no laboratory measurement of scatter or the total spot energy, the normalization of the tomography EE data is based on the OSAC calculation (Section 4). Additional EE measurements were made at $\lambda = 184.9$ nm with pinhole apertures mounted in front of the PMT in place of the KE (Fig. 6). These data are independently normalized and agree well with the results of the tomography method but have large systematic errors associated with focus and centering on the return beam in x and y . The error bars displayed in Fig. 6 for these pinhole EE data reflect the variation in signal with $\sim 1\sigma$ error in focus and centering.

This scheme for image dissection proved to be a fast, cost-effective alternative to our using other two-dimensional, UV-sensitive detectors.

4. Modeling and Interpretation

OSAC was developed to model the effects of surface irregularities on imaging performance across the entire range of spatial frequencies—from aperture diffraction and large-scale figure errors to small-scale microroughness. The scattering physics and ap-

Table 3. Input Parameters for the PSD Models [Eq. (2)] Used in the OSAC Scatter Calculation

Mirror	Low-Frequency Model			High-Frequency Model		
	σ^2 (mm ²)	b	f_0 (mm ⁻¹)	σ^2 (mm ²)	b	f_0 (mm ⁻¹)
Spare	4.94×10^{-11}	3.55	6.67×10^{-3}	2.19×10^{-12}	2.52	8.60×10^{-2}
LiF2	4.94×10^{-11}	3.55	6.67×10^{-3}	5.11×10^{-12}	2.19	8.60×10^{-2}

proximations associated with this version of OSAC are discussed elsewhere.¹²

Small-scale mirror surface errors remove energy from the central regions of the PSF, which is dominated by aperture diffraction and geometric broadening, and displace it to large angles from specular. OSAC traces rays through a system and calculates a scatter function for each surface using scalar diffraction theory. The geometric spot is then convolved with this scatter component at the image plane to form the final system PSF. OSAC accepts optical surface irregularity input as either surface autocovariance (ACV) or PSD functions or as a periodic grating surface.

A. Prefabrication Modeling

We performed an OSAC calculation prior to mirror fabrication to verify that the surface error specifications would produce mirrors meeting the imaging requirement (Section 1).¹⁸ This OSAC run used an exponential ACV model for the scatter calculation that matched the fabrication specifications in terms of rms surface error (Table 1). The assumption of an exponential ACV function is well supported.^{32,33}

The calculation verified that mirrors meeting the fabrication specifications (Table 1) would meet the EE requirement and, furthermore, that the EE would drop to only 85% at a diameter of 0.5 arc sec. That is, the FUV PSF would have a more concentrated core and broad, low-level wings. The shape of the FUV EE curve was also explored as a function of rms mid-frequency error, microroughness, and ACV function correlation length to guide decisions concerning when to stop fabrication work based on metrology data.

B. Postfabrication Modeling

The mirrors essentially met their fabrication specifications on delivery from Tinsley (Table 1). After assembly at JHU and environmental testing, all five mirrors had a rms figure error of approximately a factor of 2 greater than the fabrication specification. The rms midfrequency error and microroughness for the spare and the SiC-coated flight mirrors are approximately a factor of 2 better than the fabrication specification, whereas those values for the LiF-coated flight mirrors are somewhat worse but are still within specification.

The ray trace calculation for the postassembly OSAC modeling uses a 37 Zernike polynomial fit, $S(r)$ [Eq. (5)], to the mirror optical path difference map, $s(r, \theta)$ (Fig. 1). Features in the residual map, $s(r, \theta) - S(r)$, as well as midfrequency error and microroughness, are assigned to scatter through a fit [Eq.

(2)] to the composite PSD associated with these data (Fig. 2). The OSAC scatter calculation derives the scatter component of the PSF directly from the PSD fit [Eq. (2)] and assumes that the scatter is azimuthally symmetric. We did not model the effect of the peak in the LiF2 PSD at $\log f \approx -1.05$ (f is in units of inverse millimeters; Section 2), but we estimated its effect by scalar diffraction theory for a gratinglike surface (Subsection 4.D).³⁴

The figure error PSD associated with the distorted mirrors has a slope significantly worse than the line that best describes the midfrequency and microroughness data (Fig. 2). The PSD most representative of the postassembly mirrors was therefore best represented by a two-component model, where each component is described by Eq. (2). The fit was made in the frequency range $\log f = -2.3$ to $\log f = 2.7$, covering the surface errors that were expected to scatter energy outside the central core of the image. The parameters for the PSD models are listed in Table 3. The models were forced to yield the measured rms roughness in the midfrequency and microroughness frequency bands. All the mirrors have essentially the same postassembly figure error, so the PSD fit is the same at low spatial frequencies. However, the spare and the LiF2 have different midfrequency error and microroughness (Table 1), so the fits differ at high spatial frequencies (Table 3). The fit to the spare's PSD is characteristic of the two SiC-coated flight mirrors; and the PSD fit for LiF2 is well matched to LiF1, the other Al:LiF-coated flight mirror. This modeling therefore represents all five FUSE mirrors.

The PSD models used here are consistent with the ACV model described in Subsection 4.A: The ACV and PSD are Fourier-transform pairs, and the PSD calculated from an exponential ACV model falls off as f^{-3} (i.e., $b = 3$), which is close to the average b value for each mirror (Table 3).

C. Modeling the Image Test

The KE detector in the image test setup (Fig. 3) was focused such that the width of the tight core of the return spot was minimized and the shoulder was placed almost fully to one side of the core, emphasizing this feature (Fig. 4). The choice of focus for each image test was inconsistent and did not optimize the EE curve derived from the laboratory data [Eq. (9)], hindering a direct comparison of data between wavelengths. For example, the EE curve for the $\lambda = 435.8$ -nm test is broader than that for the UV tests because the focus was worse. The optimal OSAC focus location is based on our minimizing the rms

Table 4. Image Test Focus and Alignment

Wavelength (nm)	Defocus (μm)	R_x^a (arc sec)	R_y^b (arc sec)
435.8	123	60	30
253.7	30	60	0
184.9	45	7	45

^a R_x is rotation about the x axis (tip in y).

^b R_y is rotation about the y axis (tilt in x).

spot size and is therefore different from the choice made in the laboratory. We added different amounts of defocus to the model to reproduce the LSF data from each image test (Table 4). These values are consistent with laboratory estimates of defocus. Experiments with the OSAC model indicated that the effect of figure error on spot geometry was well sampled in spite of the defocus (see below).

The alignment stability of the optical setup was a significant obstacle. The spare was supported from the bottom edge of the rectangular substrate by two ball supports.¹⁹ The mirror tipped backward about these support points during the test, mostly rotating about the x axis, at approximately 15 arc sec/h (a rate that slowed with time). Each image test lasted approximately 5 h, and we partially compensated for the drift by tipping the mirror forward before the image test so that the mirror would drift through best alignment during the test. The effect of this misalignment was to broaden the LSF's taken later in the image test with coma and defocus (15 arc sec of tip yields approximately 15 μm of defocus). To verify that the effect of figure error could be detected behind the given amount of misalignment, we performed additional modeling of the $\lambda = 435.8\text{-nm}$ test with a perfect mirror surface, plus misalignment and defocus. The resulting EE curve is significantly different (Fig. 6).

We accommodated the finite source size (Subsection 3.A) by convolving the OSAC output with a simplified model of the source on the image plane. This noticeably changed the shape of the OSAC EE and LSF output but was also negligible compared with the effect of figure error.

The OSAC model output and associated data set for each image test are shown in Fig. 6. The slight disagreement apparent in the EE curves for $\lambda = 253.7, 184.9\text{ nm}$ at approximately 20–30 μm is attributable to the distortion (from the tip and defocus mentioned above) of a subset of the LSF's taken later during an image test (e.g., $i = n - 2, n - 1, n$). This disagreement is less evident for the $\lambda = 435.8\text{-nm}$ EE data because the detector defocus was from the outset much larger than that for the other image tests. These systematic effects are well understood, and the agreement in the LSF and EE curves (Figs. 4 and 6, respectively) validates our treatment of figure error in the modeling.

The KE step size was 5 μm for the $\lambda = 184.9\text{-nm}$ test, which smoothed the image (Fig. 4). The $\lambda = 253.7\text{-nm}$ test, with a step size of 1 μm , gives the best

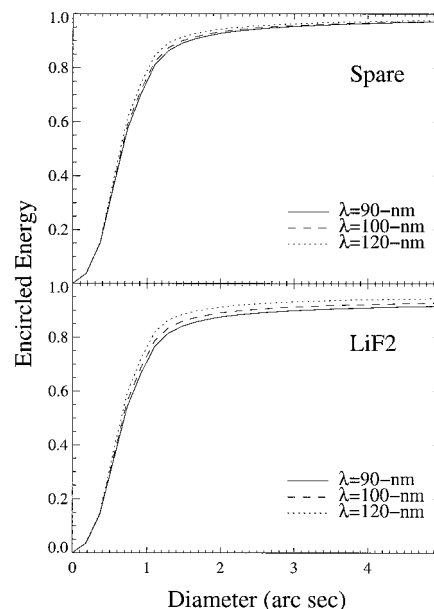


Fig. 7. Modeled single-pass EE for the spare and the LiF2 as a function of FUV wavelength. The curves for the two mirrors are similar in the core, where figure error is dominant, and differ in the wings, where scatter is important.

comparison of the data and the model in terms of spatial resolution and sensitivity.

D. Single-Pass Performance

The OSAC EE prediction for the mirrors in single pass is shown in Fig. 7. The spare and the LiF2 have $90\% \pm 5\%$ and $86\% \pm 5\%$ EE, respectively, at a diameter of 1.5 arc sec at $\lambda = 100\text{ nm}$. The quoted error is based on the uncertainty in the stability of mirror figure error and the effect of the $\log f \approx -1.05$ peak in the PSD (Section 2). Figure error instability like that observed in the laboratory should broaden or narrow the core of the EE curve (diameters of approximately <1 arc sec), but the EE at 1.5 arc sec should vary by $<5\%$. The $\log f \approx -1.05$ peak in the PSD scatters energy in first order to a diameter of approximately 3.7 arc sec [approximation (3)]. This feature should decrease the EE at 1.5 arc sec by $\sim 1\%$,³⁴ and the effect should differ for each mirror. Mid-frequency error and microroughness vary in severity across each mirror (Table 1), but this should not significantly alter the EE curve given that it azimuthally samples the PSF.

Within the systematic errors discussed above, the SiC-coated mirrors, best represented by the spare, should meet the subsystem EE requirement (Section 1) despite the increased postassembly figure error. The effect of the greater assembly-induced figure error is to broaden the EE curve for inner diameters (<1 arc sec), but the EE at 1.5 arc sec is not greatly reduced. A surface plot of the OSAC-predicted PSF for the spare at $\lambda = 100\text{ nm}$ is shown in Fig. 8.

The Al:LiF-coated mirrors, represented by LiF2, fall just short of the subsystem EE requirement, but this will have only a small effect on the performance

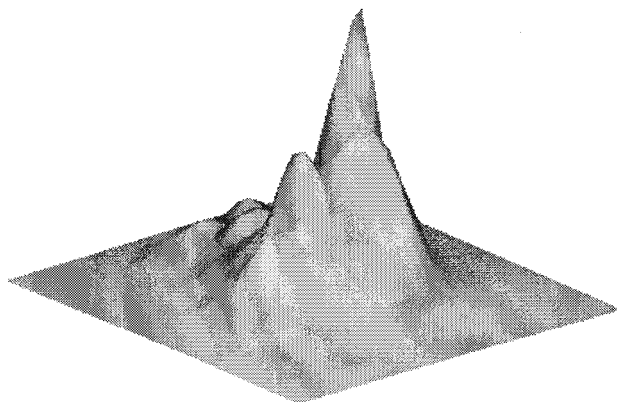


Fig. 8. PSF for the spare in single pass at $\lambda = 100$ nm. Note the compact core and broader shoulder consisting of several low peaks (~ 1.6 arc sec \times 1.6 arc sec field). The faint wings associated with scatter are not apparent on this linear scale.

of the instrument. The Al:LiF mirrors, like the SiC mirrors, have a figure error greater than the fabrication specification, but they also have a greater small-scale error than the SiC mirrors (Table 1). The scattering associated with the greater small-scale surface error decreases the EE for diameters ~ 1.5 arc sec and greater.

OSAC enlitted energy predictions for the HIRS and MDRS and instrument-level requirements are listed in Table 5 for $\lambda = 100$ nm. These enlitted energy predictions vary by approximately 1% with wavelength over the FUSE bandpass. All the flight mirrors will easily meet the HIRS transmission requirement. The Al:LiF-coated mirrors may not quite meet the MDRS requirement. These numbers include the effect of spacecraft pointing error as indicated. The current estimate of pointing jitter is approximately 0.4 arc sec FWHM. Mirror misalignments on the instrument optical bench were not included in this calculation because they are small and have a negligible influence on the spot size.³⁵ The effect of the peak at $\log f \approx -1.05$ (f is in units of inverse millimeters) in the PSD should decrease HIRS transmission by $<1\%$. This feature should have even less effect on MDRS transmission. The on-orbit mirror PSF is expected to improve instrument resolution by approximately 5% from the values measured during laboratory spectrograph alignment and characterization.³⁶

Table 5. Modeled On-Orbit Slit Transmission at $\lambda = 100$ nm^a

Mirror Pair	FWHM _{jitter} (= 0.25 arc sec)		FWHM _{jitter} (= 0.5 arc sec)	
	HIRS (%)	MDRS (%)	HIRS (%)	MDRS (%)
Requirement	50	95	50	95
SiC coated	92	98	89	98
LiF coated	88	93	85	93

^aThe systematic errors discussed in Subsection 4.D limit the accuracy of these values to approximately $\pm 5\%$.

In a future paper we will discuss in-flight performance of the mirror assemblies.

5. Conclusion

The OSAC package, developed for other short-wavelength space astronomy programs,^{12,37–39} was used to check FUSE mirror fabrication specifications that were based on the Solar Ultraviolet Measurements of Emitted Radiation program heritage. We performed laboratory image testing to verify performance and validate the OSAC model using mirror metrology data. We used the validated model based on surface error measurements to predict on-orbit, FUV spectrograph slit transmission.

The FUSE mirrors will easily meet the instrument-level requirement for spectrograph HIRS transmission, and the two SiC-coated mirrors will meet the requirement for MDRS transmission (Table 5). The Al:LiF-coated mirrors should fall short of the MDRS requirement by approximately $<1\sigma$ (i.e., $<5\%$) in our calculation of slit transmission (Table 5). This shortcoming will have an almost negligible influence on overall instrument sensitivity and spectral resolution.

We completed a program of testing and modeling the mirrors for the FUSE telescope under a tight budget and challenging schedule. The image test showed that there were no severe problems with the flight mirrors, and the implications of surface metrology were understood. The long-term development of analysis tools for understanding optical performance in the FUV for other astronomy missions has been critical to the complete interpretation of our results.

We gratefully acknowledge James Harvey of the Center for Research and Education in Optics and Lasers at the University of Central Florida, Keith Peacock of the JHU Applied Physics Laboratory, and Steven Conard of the JHU Instrument Development Group for their contributions to the development of mirror fabrication specifications; David Content of the NASA Goddard Space Flight Center for his assistance with mirror metrology; and the FUSE team at Tinsley for their advice and hard work. This research is supported by NASA contract NAS5-32985.

References and Notes

1. H. W. Moos *et al.*, "Overview of the Far Ultraviolet Spectroscopic Explorer mission," *Astrophys. J.* (in press).
2. D. J. Sahnou, S. D. Friedman, H. W. Moos, J. C. Green, and O. H. Siegmund, "Preliminary performance estimates for the Far Ultraviolet Spectroscopic Explorer (FUSE)," in *Space Telescopes and Instruments V*, P. Y. Bely and J. B. Breckinridge, eds., Proc. SPIE **3356**, 552–560 (1998).
3. D. J. Sahnou *et al.*, "On-orbit performance of the Far Ultraviolet Spectroscopic Explorer (FUSE) satellite," *Astrophys. J.* (in press).
4. M. J. Kennedy, S. D. Friedman, R. H. Barkhouser, J. Hampton, and P. Nikulla, "Design of the Far Ultraviolet Spectroscopic Explorer mirror assemblies," in *Space Telescopes and Instruments IV*, P. Y. Bely and J. B. Breckinridge, eds., Proc. SPIE **2807**, 172–183 (1996).
5. W. R. Hunter, J. F. Osantowski, and G. Hass, "Reflectance of aluminum overcoated with MgF₂ and LiF in the wavelength

- region from 1600 Å to 300 Å at various angles of incidence,” *Appl. Opt.* **10**, 540–544 (1971).
6. R. A. M. Keski-Kuha, J. F. Osantowski, H. Herzig, J. S. Gum, and A. R. Toft, “Normal incidence reflectance of ion beam deposited SiC films in the EUV,” *Appl. Opt.* **27**, 2815–2816 (1988).
 7. R. A. M. Keski-Kuha, J. I. Larruquert, J. S. Gum, and C. M. Fleetwood, “Optical coatings and materials for ultraviolet space astronomy,” in *Ultraviolet-Optical Space Astronomy Beyond HST*, J. A. Morse, J. M. Shull, and A. L. Kinney, eds., *Astronomical Society of the Pacific Conference Series* **164**, 406–419 (1999).
 8. FUSE Instrument and Science Operations Team, “FUSE instrument requirements document,” FUSE-JHU-0004, Rev. B (Johns Hopkins University, Baltimore, Md., 1996).
 9. Silicon Valley Group, Inc., Tinsley Division, Tinsley Laboratories, 3900 Lakeside Drive, Richmond, Calif. 94806.
 10. R. G. Ohl, R. H. Barkhouser, M. J. Kennedy, and S. D. Friedman, “Assembly and test-induced distortions of the FUSE mirrors—lessons learned,” in *Space Telescopes and Instruments V*, P. Y. Bely and J. B. Breckinridge, eds., *Proc. SPIE* **3356**, 854–865 (1998).
 11. R. J. Noll, P. Glenn, and J. F. Osantowski, “Optical surface analysis code (OSAC),” in *Scattering in Optical Materials II*, S. Musikant, ed., *Proc. SPIE* **62**, 78–82 (1983).
 12. T. T. Saha, D. B. Leviton, and P. Glenn, “Performance of ion-figured silicon carbide SUMER telescope mirror in the vacuum ultraviolet,” *Appl. Opt.* **35**, 1742–1750 (1996).
 13. R. G. Ohl, S. D. Friedman, T. T. Saha, R. H. Barkhouser, and H. W. Moos, “Optical testing of the Far Ultraviolet Spectroscopic Explorer primary mirrors and predicted on-orbit performance,” in *EUUV, X-Ray and Gamma-Ray Instrumentation for Astronomy X*, O. H. Siegmund and K. A. Flanagan, eds., *Proc. SPIE* **3765**, 482–494 (1999).
 14. J. E. Harvey and A. Kotha, “Scattering effects from residual optical fabrication errors,” in *International Conference on Optical Fabrication and Testing*, T. Kasai, ed., *Proc. SPIE* **2576**, 155–174 (1995).
 15. J. C. Stover, *Optical Scattering, Measurement and Analysis*, Vol. PM24 of SPIE Monograph Series (SPIE Press, Bellingham, Wash., 1995).
 16. J. M. Bennett and L. Mattson, *Introduction to Surface Roughness and Scattering*, 2nd ed. (Optical Society of America, Washington, D.C., 1999), pp. 62–86.
 17. P. Glenn, “Metrology data processor (METDAT),” final report, NASA contract S-73672-E (NASA Goddard Space Flight Center, Greenbelt, Md., 1994).
 18. J. E. Harvey, “Final report for FUSE telescope performance predictions,” consulting agreement under NASA contract NAS5–32985 (Johns Hopkins University, Baltimore, Md., 1996).
 19. R. H. Barkhouser and R. G. Ohl, “Interferometric alignment and figure testing of large (0.5 m) off-axis parabolic mirrors in a challenging cleanroom environment,” in *Optical Manufacturing and Testing III*, H. P. Stahl, ed., *Proc. SPIE* **3782**, 601–614 (1999).
 20. P. Glenn, “Lambda-over-thousand metrology results for steep spheres using a curvature profiling technique,” in *Advanced Optical Manufacturing and Testing II*, V. J. Doherty, ed., *Proc. SPIE* **1531**, 54–61 (1991).
 21. R. A. M. Keski-Kuha, NASA Goddard Space Flight Center, Greenbelt, Md. (personal communication, 2000).
 22. R. A. M. Keski-Kuha, G. M. Blumenstock, C. M. Fleetwood, and D.-R. Schmitt, “Effects of space exposure on ion-beam-deposited silicon-carbide and boron-carbide coatings,” *Appl. Opt.* **37**, 8038–8042 (1998).
 23. J. F. Osantowski, R. A. M. Keski-Kuha, H. Herzig, A. R. Toft, J. S. Gum, and C. M. Fleetwood, “Optical coating technology for the EUV,” *Adv. Space Res.* **11**, 185–201 (1991).
 24. S. J. Conard, R. H. Barkhouser (Department of Physics and Astronomy, Johns Hopkins University, Baltimore, Maryland 21218), S. D. Friedman, J. W. Kruk, H. W. Moos, R. G. Ohl, and D. J. Sahnou, are preparing a manuscript to be called “The Far Ultraviolet Spectroscopic Explorer optical system: lessons learned.”
 25. A ray trace calculation assuming a perfectly parabolic mirror with this offset from nominal focus yields a rms spot radius of 0.56 μm.
 26. WYKO Model 400 interferometer, Veeco Corporation (formerly WYKO Corporation), 2650 East Elvira Road, Tucson, Ariz. 85706.
 27. WYKO Model TOPO 3-D interferometer, Veeco Corporation (formerly WYKO Corporation), 2650 East Elvira Road, Tucson, Ariz. 85706.
 28. Nu-Tek Precision Optical Corporation, 1202 Technology Drive, Suites L-P, Aberdeen, Md. 21001.
 29. J. Radon, “Über die Bestimmung von Funktionen durch ihre Integralwerte längs gewisser Mannigfaltigkeiten,” *Ber. Verh. Sächs. Akad. Wiss. Leipzig, Math.-Phy. Klasse* **69**, 262–277 (1917).
 30. S. W. Rowland, “Computer implementation of image reconstruction formulas,” in *Image Reconstruction from Projections—Implementation and Applications*, Vol. 32 of Topics in Applied Physics, G. T. Herman, ed. (Springer-Verlag, New York, 1979), pp. 9–79.
 31. R. N. Bracewell, *Two-Dimensional Imaging* (Prentice-Hall, Englewood Cliffs, N.J., 1995), pp. 505–544.
 32. R. J. Noll and P. Glenn, “Mirror surface autocovariance functions and their associated visible scattering,” *Appl. Opt.* **21**, 1824–1838 (1982).
 33. A. Slomba, R. Babish, and P. Glenn, “Mirror surface metrology and polishing for AXAF/TMA,” in *X-Ray Instrumentation in Astronomy*, J. L. Culhane, ed., *Proc. SPIE* **597**, 40–54 (1985).
 34. T. T. Saha, ed., *Optical Surface Analysis Code (OSAC), User’s Manual* (NASA Goddard Space Flight Center, Greenbelt, Md., 1993), pp. 5-74–5-76.
 35. S. J. Conard, K. W. Redman, R. H. Barkhouser, and J. A. Johnson, “Optical alignment of the Far Ultraviolet Spectroscopic Explorer,” in *EUUV, X-Ray, and Gamma-Ray Instrumentation for Astronomy X*, O. H. Siegmund and K. A. Flanagan, eds., *Proc. SPIE* **3765**, 618–629 (1999).
 36. A. N. Cha, D. J. Sahnou, and H. W. Moos, “Processing and interpretation of pre-flight FUSE spectra,” in *EUUV, X-Ray, and Gamma-Ray Instrumentation for Astronomy X*, O. H. Siegmund and K. A. Flanagan, eds., *Proc. SPIE* **3765**, 495–505 (1999).
 37. P. Glenn, “Space telescope performance prediction using the optical surface analysis code (OSAC),” *Opt. Eng.* **25**, 1026–1033 (1986).
 38. T. T. Saha, D. A. Thomas, and J. F. Osantowski, “OSAC analysis of the Far Ultraviolet Spectroscopic Explorer (FUSE) telescope,” in *Grazing Incidence Optics*, J. F. Osantowski and L. P. Van Speybroeck, eds., *Proc. SPIE* **640**, 79–84 (1986).
 39. M. D. Freeman, J. P. Hughes, L. P. Van Speybroeck, J. W. Bilbro, and M. C. Weisskopf, “Image analysis of the AXAF VETA-I x-ray mirror,” in *Multilayer and Grazing Incidence X-Ray/EUV Optics for Astronomy and Projection Lithography*, R. B. Hoover and A. B. Walker, Jr., eds., *Proc. SPIE* **1742**, 136–151 (1992).